

DMP Monitoring as a Process Optimization Tool for Direct Metal Printing (DMP) of Ti-6Al-4V

Nachiketa Ray[✉], Manisha Bisht, Lore Thijs, Jonas Van Vaerenbergh, Sam Coeck

3D Systems, Grauwmeer 14, 3001 Leuven, Belgium

Abstract

Metal Additive Manufacturing (AM) has evolved as a production technique for rapid prototyping as well as high volume precision manufacturing. In this work, DMP Monitoring, a new feature of 3D Systems' direct metal printer, ProX[®] DMP 320 has been used as a tool for process parameter optimization. The effect of the variations of process parameters like layer thickness, laser power, scan speed and hatch spacing on the physical and mechanical properties of the additively manufactured Ti-6Al-4V samples have been investigated. In addition to the conventional post-processing evaluation methods like Archimedes' density, X-ray CT and tensile testing, new in-situ process monitoring tools are assessed and compared with the traditional evaluation methods.

Keywords

Laser powder bed fusion, Ti-6Al-4V, process optimization, monitoring, X-ray CT

1. Introduction

Conventional processing of cast and wrought alloys followed by numerically controlled machining used to be an indisputable choice in the metal industry until the additive age. Additive manufacturing can be described as 'a process of joining materials to make objects from 3D model data, usually layer upon layer as opposed to subtractive manufacturing methodologies' [1]. The most commonly used metal additive technology on an industrial scale is powder bed fusion, where layer upon layer of powder is deposited on a build platform (of ideally the same material) and are fused together using a laser or electron beam. Although metal additive manufacturing has revolutionized the approach towards near net shaping, rapid prototyping and high volume precision production, the technology presents itself with its own set of challenges. One of the challenges to transfer this technology from prototyping to volume production is to ensure part quality [2]. Therefore, process optimization is an integral part of the technology, since it determines the stability of the process and reinforces assurance amongst the users regarding the reproducibility of part quality.

Titanium is one of the metals with high specific strength (ratio of strength to density) amongst the naturally occurring elements and combined with its excellent corrosion resistance makes it an appropriate candidate for state-of-the-art applications. Ti-6Al-4V is the most widely used Ti alloy as it accounts for more than 50% of Ti usage in the world [3,4]. It is challenging to produce Ti-6Al-4V components using conventional means. Castings for this alloy costs 2-3 times the cost of superalloy castings due to specific process conditions, forging is unable to produce complex shapes and powder metallurgy processes usually result in lower mechanical properties [5,6]. As a result, laser based powder bed fusion has become popular and has led to extensive research regarding the use of Ti-6Al-4V processing, especially for aerospace and biomedical applications [7–12].

Process parameter optimization of Ti-6Al-4V powder bed fusion in order to achieve near theoretical density has been of considerable interest in both experimental [13,14] and

✉ nachiketa.ray@3dsystems.com

modelling [15] techniques. Sometimes the experimental methods come across process instabilities which lead to defects in the as-printed components like porosity (lack of fusion, key holes and gas pores), cracks and warpage in addition to the expected homogeneously distributed porosities (caused by non-optimal process parameters) [16–19]. This stochastic nature of the process has led to a lot of research in the field of in-situ process control and monitoring using various methodologies [20–24] in order to track down defect formation during the process and mitigate the risk of failure during application. However in this work, DMP Monitoring, a new feature of 3D Systems’ direct metal printer, ProX[®] DMP 320 has been used as a process optimization tool instead of a process control technique. Ex-situ characterization techniques like density, X-ray CT and mechanical properties are compared with the data collected by DMP Monitoring.

2. Experiments

Atomized Ti-6Al-4V ELI (extra low interstitial grade) powder having a chemical composition which complies with ASTM F3001 and ASTM B348 (LaserForm[®] Ti Gr23 [25]) was additively manufactured in a commercial ProX[®] DMP 320 from 3D Systems. The direct metal printer (DMP) is shown in **Fig 1** (a) and the three basic components of the laser powder bed fusion setup are shown in **Fig 1** (b). It consists of an optical system guiding the laser beam in order to selectively melt the powder, a build envelope in combination with the powder deposition unit and the DMP Monitoring suite. The optical system is equipped with a 500 W Ytterbium fiber laser, having a wavelength of 1070 nm, which is guided and focused on the build envelope using galvanometer scanning mirrors and $f - \theta$ lens respectively. The build envelope is 275×275 mm in the X-Y plane and travels in Z up to 420 mm. The Z travel after each scanned layer determines the layer thickness (LT [μm]) of the process. The powder which is stored in two feedstocks placed on the left and right of the build envelope is uniformly deposited using a scraper from both sides every alternate layer.

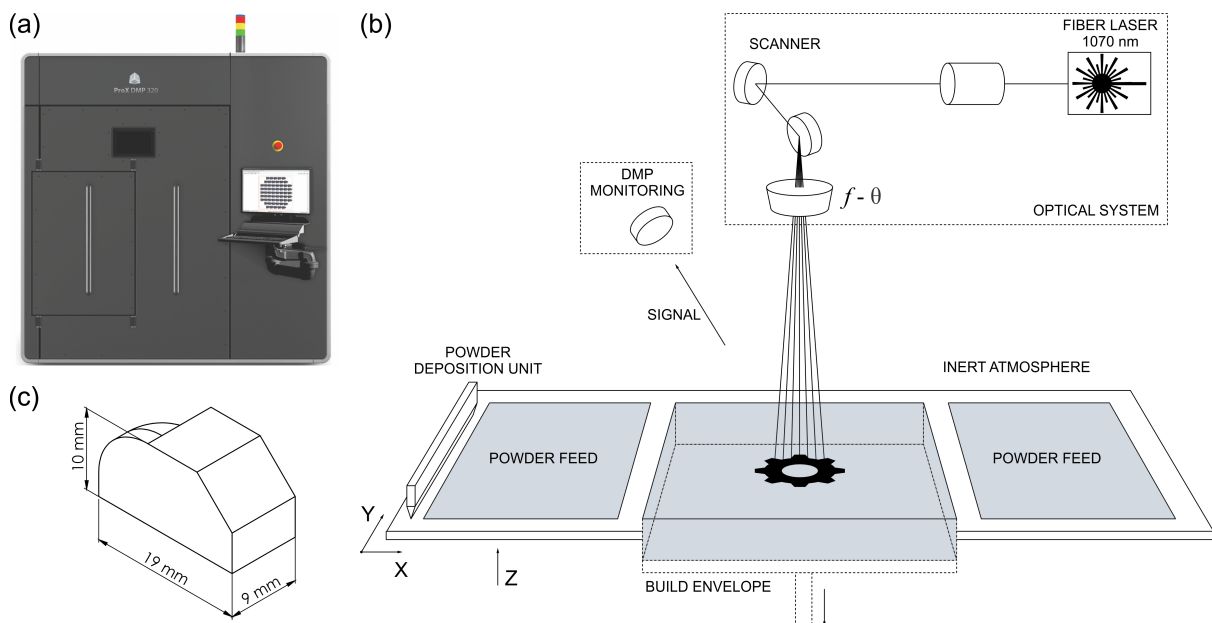


Fig 1. (a) ProX[®] DMP 320 (b) Schematic illustrating the laser powder bed fusion process in a ProX[®] DMP 320 (c) Design of the blocks additively manufactured in this work.

The DMP Monitoring suite comprises of DMP Vision and DMP Meltpool. DMP Vision is a camera used to capture images every layer post scanning and deposition. DMP Meltpool is used to monitor the light intensity emitted from the process using an off-axis Ge photodiode

in real time, details of which can be found in our previous work [26]. An example of the signal acquired by DMP Monitoring during the direct metal printing process is shown in **Fig 2** where it synchronizes the data collected after every layer for aided visualization.

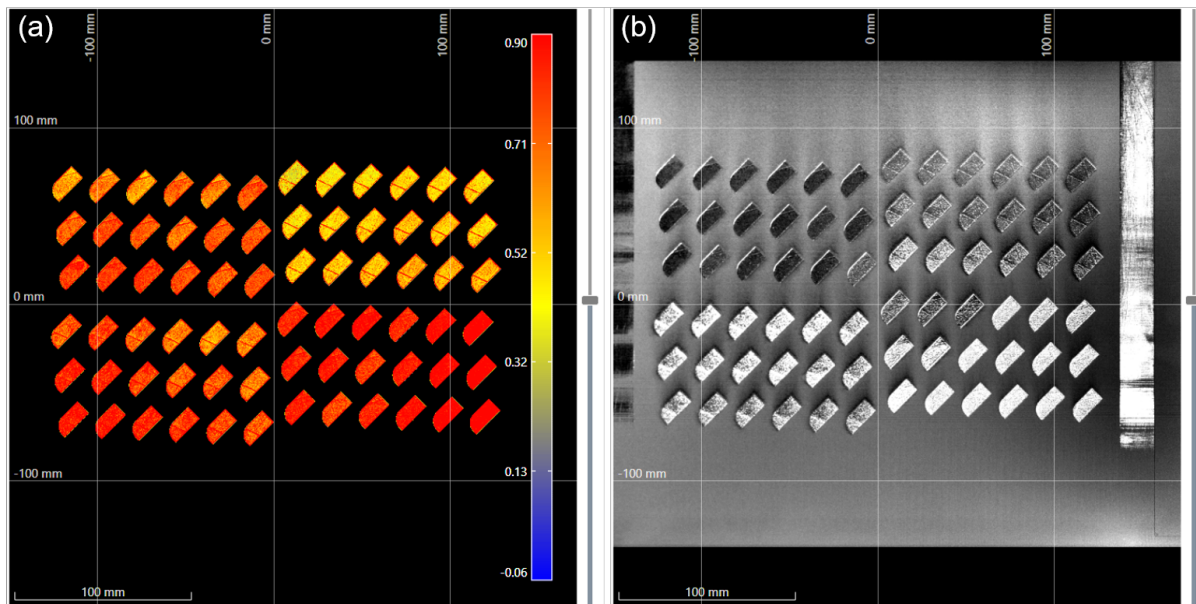


Fig 2. DMP Monitoring user interface (UI) showing DMP Meltpool (a) and DMP Vision (b) acquisition in real time for a given layer. The DMP Meltpool bitmap is a false color image with the color representative of the observed intensity.

In this work, two layer thicknesses (LT [μm]) of $30\mu m$ and $60\mu m$ were chosen to print the blocks having dimensions as shown in **Fig 1** (c). Blocks of each layer thickness were printed with varying laser power (P [W]) and scan velocities (v_s [$mm \cdot s^{-1}$]) having a constant hatch spacing (H_s [μm]). The variations in laser power (90% - 140% of the standard) and scan speed (75% - 250% of the standard) were made accordingly to have an increasing amount of volumetric energy density (VED), which can be defined as the average energy imparted per unit volume on the powder bed [27–29] as shown in **Eq. (1)**.

$$VED = \frac{P}{LT \cdot v_s \cdot H_s} \times 10^6 [J \cdot mm^{-3}] \quad (1)$$

The density of all the blocks were measured using Archimedes' principle. Two samples from each layer thickness were chosen to be scanned with X-ray computed tomography (CT) in a Phoenix Nanotom (GE) with a voxel size of approximately $15\mu m$ to calculate the amount of porosity in the blocks. VGSTUDIO MAX (Volume Graphics) was used for data analysis.

The DMP Meltpool data was acquired by the detector and logged as a function of time and the data analysis was carried out separately and is not a part of the collection software (**Fig 2**). The data analysis as a function of time is non-trivial and also impractical. On the contrary, mapping the signal intensity as a function of spatial coordinates on the powder bed is much more comprehensible. The X and Y coordinates of the laser position at the powder bed level were logged every $20 \mu s$ along with its corresponding total emitted intensity acquired over those $20 \mu s$. The DMP Meltpool data (which contains the X, Y, Z co-ordinates and the corresponding intensity recorded by the photo diode) for each layer was stored in a separate file and was analyzed using an algorithm which detects the intensity fluctuations above a certain threshold and over a certain spatial range and tags them as DMP Meltpool events. The

criteria for DMP Meltpool events detection were based on holistic rules established in our previous study [26]. The probability of a DMP Meltpool event resulting into a defect is higher if it manifests itself in more than one layer in the vicinity of the same XY co-ordinate. The volume of each DMP Meltpool event (v_i), was added up for all the events following the above criteria (n), and the ‘DMP Meltpool event to part volume ratio’ (ρ_m) was calculated using Eq. (2). Each Ti-6Al-4V block having a volume, V was analyzed individually in this work.

$$\rho_m = \frac{\sum_{i=1}^n v_i}{V} \times 100\% \quad (2)$$

Near net shaped round tensile test coupons were printed in the direction perpendicular to the build platform with the same process parameters as the four blocks selected for X-ray CT analysis. No heat treatment or surface finishing was carried out for the tensile coupons prior to testing. For each process parameter set, six samples having dimensions as recommended by ASTM E8M [30] with a gauge diameter of 4mm were printed. Room temperature tensile tests were performed according to ASTM E8M on the as-built samples with a strain rate of 0.005 min^{-1} in the elastic regime and 0.4 min^{-1} in the plastic regime.

3. Results and discussion

After the direct metal printing process, the blocks were detached from the Ti build platform, and the density of each block was measured using Archimedes’ principle and is shown in **Fig 3** as a function of volumetric energy density (a, b) and scan velocity (c, d) for both layer thicknesses. The theoretical density was taken as 4.42 $\text{g}\cdot\text{cm}^{-3}$ and it can be seen that the relative density never goes above 99.3%. This can be attributed to the measurement method [31] and in order to verify that, the pixel density of one of the samples with the highest Archimedes’ density was measured on a grinded and polished cross-section which corresponded to a value of 99.97% for an Archimedes density of 99.35%. It should be noted that the relative density increases with increasing VED, but above a certain value, depending on the layer thickness, the relative density achieves a stable value. The initial low value of density can be attributed to porosity caused by lack of fusion as a result of insufficient overlap between the melt pools. Further increasing the VED does not reflect any drastic changes in density measured by Archimedes’ principle for LT30 (**Fig 3** (a)), but a small drop in density is observed for LT60 (**Fig 3** (b)) which can be associated with the formation of keyhole porosities.

The calculated ρ_m for the blocks are also plotted as a function of VED in **Fig 3** (a, b). For the layer thickness 30 μm , no trend was observed, however for layer thickness 60 μm the ρ_m decreases with increasing VED. It should be noted that the ρ_m does not correspond to the volume fraction of porosity, but acts as a mere indication of the volume fraction of pores. However, it’s interesting to note that although the relative density remains constant for LT60 above VED of 30 $\text{J}\cdot\text{mm}^{-3}$, the ρ_m value decreases up to 40 $\text{J}\cdot\text{mm}^{-3}$ and then becomes stable. This would be an indication that at least VED of 40 $\text{J}\cdot\text{mm}^{-3}$ is required to achieve near theoretical density. As mentioned before, the current analysis requires an abrupt fluctuation in the DMP Meltpool signal of adjacent vectors which persists for consecutive layers to flag an event, which is not expected to be observed in the signature of a keyhole. In order to compare the volume fraction of events detected by DMP Meltpool with the actual porosity fraction, X-ray CT analysis was performed on two samples with high Archimedes’ density from each layer thickness, one with low and high ρ_m . The measured porosity fraction for the four samples are indicated in **Fig 3** (a, b) and its corresponding ρ_m is highlighted. Both the ρ_m and the CT pore to part volume ratio appear to follow a similar trend but the absolute values should not be compared as mentioned before.

In **Fig 3** (c, d) both the relative density and ρ_m are plotted as a function of increasing scan velocity. Multiple data points for a given velocity value are due to differences in laser power. The range of the X axes in both **Fig 3** (c) and (d) are kept identical in order to provide some reference to the reader. Again for LT30, no clear trend is observed, while for LT60 the ρ_m increases with increase in scan velocity. This provides an indication that if a process parameter set is chosen just based on the Archimedes' density, parameters with higher scan velocity have a significant chance of having more events than parameter sets with lower scan velocity. However, it should be taken into account that all the data points shown in **Fig 3** (d) have different values of VED. In order to have a more accurate perspective, two interesting VED ranges for the layer thickness of 60 μm have been considered and their corresponding relative density and ρ_m have been plotted against the scan velocity in **Fig 4**. For the sake of comparison, the scale has been kept identical to **Fig 3** (d). It can be perceived that for high VED $\sim 40 \text{ J}\cdot\text{mm}^{-3}$, which also corresponds to lower scan velocities, no trend in ρ_m can be observed. However, for low VED $\sim 30 \text{ J}\cdot\text{mm}^{-3}$, corresponding to higher scan velocities, ρ_m increases with increasing scan velocities. This again leads to the fact that DMP Meltpool is not only suitable for detecting lack of fusion porosities caused by low VED (predictable) but also defects which form randomly.

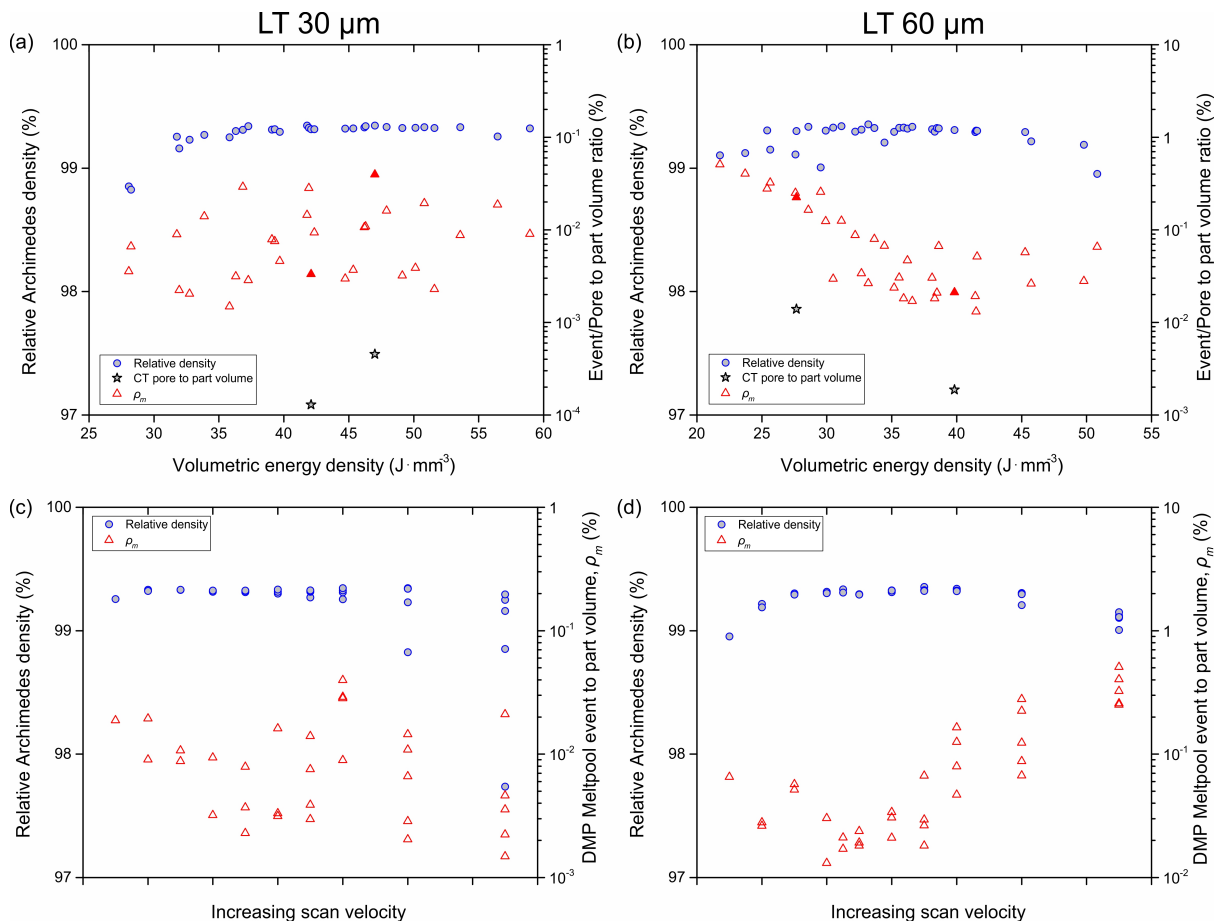


Fig 3. Relative theoretical density measured using Archimedes' method and its corresponding event to part volume ratio (%) is shown as a function of the volumetric energy density applied during the powder bed fusion process for layer thickness 30 μm (a) and 60 μm (b). The ratio of the pore to part volume (%) measured by CT is also indicated in (a) and (b) and its corresponding event to part volume is highlighted. (c) and (d) illustrate the relative density and event to part volume ratio (%) as a function of increasing scan velocity for layer thickness 30 μm and 60 μm respectively.

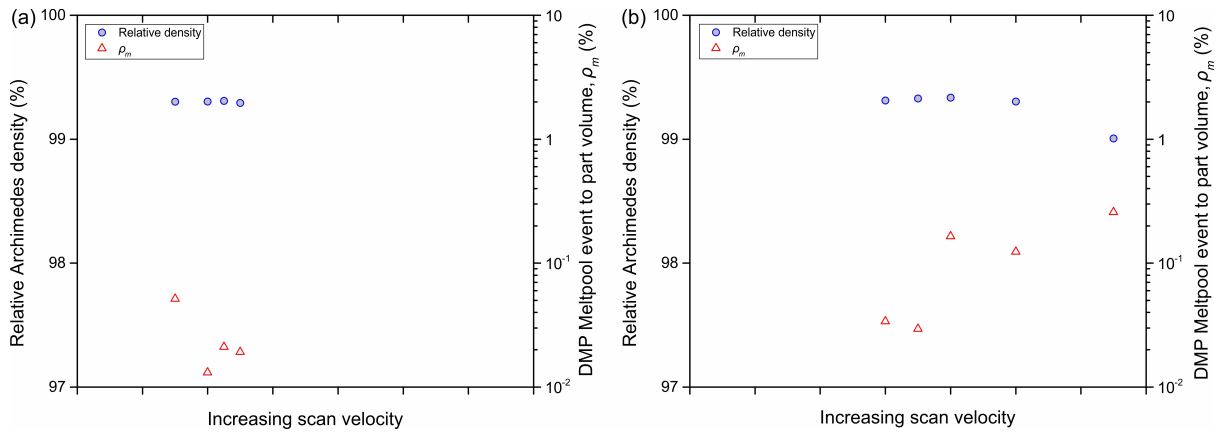


Fig 4. Relative density and event to part volume ratio (%) as a function of increasing scan velocity for layer thickness 60 μm plotted in the same scale as **Fig 3** (d) for VED range (a) 38-42 $\text{J}\cdot\text{mm}^{-3}$ and (b) 28-32 $\text{J}\cdot\text{mm}^{-3}$.

Room temperature tensile testing was carried on the as-built coupons printed with the same process parameters as the four blocks selected for X-ray CT analysis. The yield strength (YS), ultimate tensile strength (UTS) and the plastic strain were calculated from the stress-strain curves and the average and 2σ (twice the standard deviation) of six tests for the four process parameters are summarized in **Fig 5**.

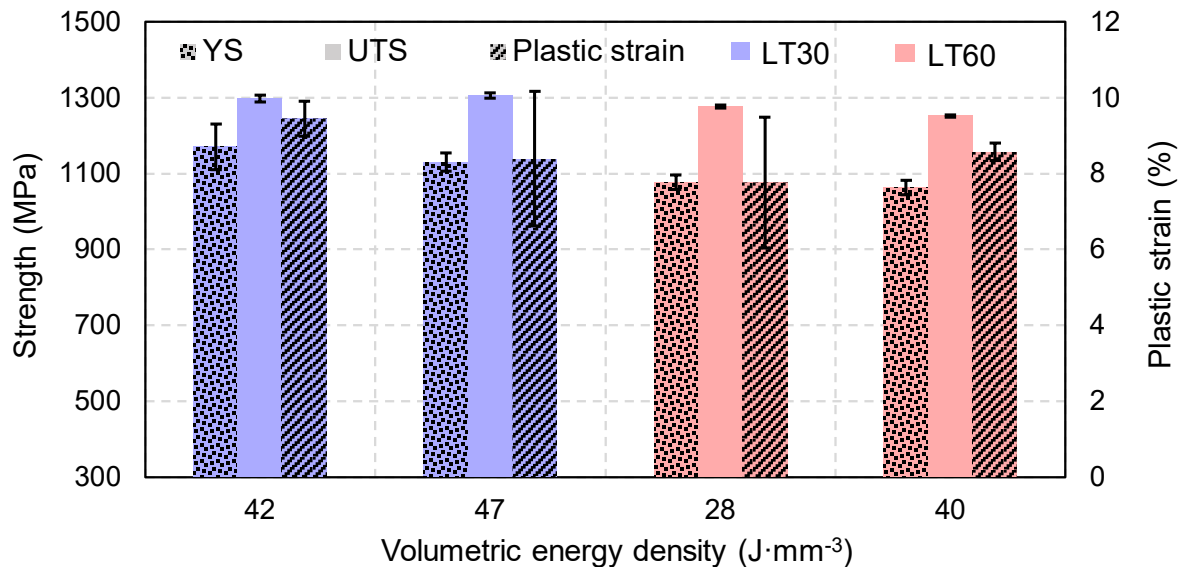


Fig 5. Room temperature tensile properties of as-built samples printed in the direction perpendicular to the build platform for layer thickness 30 μm and 60 μm , having the same laser parameters as the samples highlighted in **Fig 3** (a) and (b). The four process parameters also correspond to the blocks selected for X-ray CT analysis.

It is well known from literature that the microstructure of as-printed, non-heat treated Ti-6Al-4V consists of fine acicular martensite (α') as a result of the high cooling rates characteristic of the process [12,27]. As a result of which direct metal printed Ti-6Al-4V tend to have high yield and tensile strength but relatively low ductility [32–34]. Small changes in porosity are directly reflected in the ductility of the as-printed material [17]. The plastic strain observed in **Fig 5** for a given layer thickness and VED is consistent with the CT pore to part volume ratio and ρ_m as shown in **Fig 3** (a) and (b). With increasing porosity or DMP Meltpool events, the plastic strain decreases. It is important to note that a higher VED may not correspond

to lower porosity levels. Although the relative density measured using Archimedes' principle for LT30 is comparable for VED of 42 and 47 J·mm⁻³, the plastic strain, CT density and DMP Meltpool density ($1 - \rho_m$) were all lower for the samples printed with the higher VED (47 J·mm⁻³). It was also observed that samples with higher CT pore to part volume ratio and ρ_m had a large scatter in the plastic strain data for both layer thicknesses. Therefore, solely from this work it is the intention of the authors to adopt ρ_m as an indication or possibility of defect formation rather than a measure of porosity since further verification and validation of the DMP Meltpool data analysis is required.

4. Conclusions

In this work, several blocks were additively manufactured by laser powder bed fusion for layer thickness (LT) of 30µm and 60µm with varying laser power and scan velocity for a constant hatch spacing. DMP Monitoring was used as an in-situ process monitoring tool to identify non-conformities during the process. Analysis of the DMP Meltpool data was compared with X-ray CT measurements performed on selected samples with similar relative density measured using Archimedes' principle. A strong correlation was observed between the DMP Meltpool event to part volume ratio (ρ_m) and the CT pore to part volume ratio. For LT30 no trend was observed between the volumetric energy density (VED) and ρ_m , however for LT60, a correlation was observed for lower VED and higher scan velocities. In order to compare with the mechanical properties, room temperature tensile tests were performed on as-built near net shape samples printed perpendicular to the build platform. The plastic strain showed a strong correlation with the CT pore to part volume ratio and ρ_m . It was shown that the VED and relative density measured using Archimedes' principle were not always a good indication for selecting process parameters required to print defect free components. DMP Monitoring was shown as a promising tool to gain confidence in part quality compared to destructive techniques like tensile testing and expensive characterization techniques like X-ray CT.

References

- [1] ASTM F2792-12a, Standard Terminology for Additive Manufacturing Technologies, ASTM Int. West Conshohocken PA. (2012). doi:10.1520/f2792-12a.
- [2] W.E. King, A.T. Anderson, R.M. Ferencz, N.E. Hodge, C. Kamath, S.A. Khairallah, A.M. Rubenchik, Laser powder bed fusion additive manufacturing of metals; physics, computational, and materials challenges, *Appl. Phys. Rev.* 2 (2015) 041304. doi:10.1063/1.4937809.
- [3] M.J. Donachie, *Titanium: A Technical Guide*, 2nd Edition, ASM International, 2000.
- [4] G. Welsch, R. Boyer, E.W. Collings, *Materials Properties Handbook: Titanium Alloys*, ASM International, 1993.
- [5] J. Alcisto, A. Enriquez, H. Garcia, S. Hinkson, T. Steelman, E. Silverman, P. Valdovino, H. Gigerenzer, J. Foyos, J. Ogren, J. Dorey, K. Karg, T. McDonald, O.S. Es-Said, Tensile Properties and Microstructures of Laser-Formed Ti-6Al-4V, *J. Mater. Eng. Perform.* 20 (2011) 203–212. doi:10.1007/s11665-010-9670-9.
- [6] H.R. Salimijazi, T.W. Coyle, J. Mostaghimi, Vacuum plasma spraying: A new concept for manufacturing Ti-6Al-4V structures, *JOM.* 58 (2006) 50–56. doi:10.1007/s11837-006-0083-z.
- [7] M.K. Thompson, G. Moroni, T. Vaneker, G. Fadel, R.I. Campbell, I. Gibson, A. Bernard, J. Schulz, P. Graf, B. Ahuja, F. Martina, Design for Additive Manufacturing: Trends, opportunities, considerations, and constraints, *CIRP Ann.* 65 (2016) 737–760. doi:10.1016/j.cirp.2016.05.004.
- [8] M. Geetha, A.K. Singh, R. Asokamani, A.K. Gogia, Ti based biomaterials, the ultimate choice for orthopaedic implants – A review, *Prog. Mater. Sci.* 54 (2009) 397–425. doi:10.1016/j.pmatsci.2008.06.004.
- [9] X. Song, L. Wang, M. Niinomi, M. Nakai, Y. Liu, Fatigue characteristics of a biomedical β -type titanium alloy with titanium boride, *Mater. Sci. Eng. A.* 640 (2015) 154–164. doi:10.1016/j.msea.2015.05.078.
- [10] K. Wang, The use of titanium for medical applications in the USA, *Mater. Sci. Eng. A.* 213 (1996) 134–137. doi:10.1016/0921-5093(96)10243-4.
- [11] E. Uhlmann, R. Kersting, T.B. Klein, M.F. Cruz, A.V. Borille, Additive Manufacturing of Titanium Alloy for Aircraft Components, *Procedia CIRP.* 35 (2015) 55–60. doi:10.1016/j.procir.2015.08.061.
- [12] D. Agius, K.I. Kourousis, C. Wallbrink, A Review of the As-Built SLM Ti-6Al-4V Mechanical Properties towards Achieving Fatigue Resistant Designs, *Metals.* 8 (2018) 75. doi:10.3390/met8010075.
- [13] G. Kasperovich, J. Haubrich, J. Gussone, G. Requena, Correlation between porosity and processing parameters in TiAl6V4 produced by selective laser melting, *Mater. Des.* 105 (2016) 160–170. doi:10.1016/j.matdes.2016.05.070.
- [14] L. Thijs, B. Vrancken, J.-P. Kruth, J.V. Humbeeck, The Influence of Process Parameters and Scanning Strategy on the Texture in Ti6Al4V Parts Produced by Selective Laser Melting, in: 2013.
- [15] I. Baturynska, O. Semeniuta, K. Martinsen, Optimization of Process Parameters for Powder Bed Fusion Additive Manufacturing by Combination of Machine Learning and Finite Element Method: A Conceptual Framework, *Procedia CIRP.* 67 (2018) 227–232. doi:10.1016/j.procir.2017.12.204.
- [16] H. Shipley, D. McDonnell, M. Culleton, R. Coull, R. Lupoi, G. O'Donnell, D. Trimble, Optimisation of process parameters to address fundamental challenges during selective laser melting of Ti-6Al-4V: A review, *Int. J. Mach. Tools Manuf.* 128 (2018) 1–20. doi:10.1016/j.ijmachtools.2018.01.003.

- [17] M. Schmidt, M. Merklein, D. Bourell, D. Dimitrov, T. Hausotte, K. Wegener, L. Overmeyer, F. Vollertsen, G.N. Levy, Laser based additive manufacturing in industry and academia, *CIRP Ann.* 66 (2017) 561–583. doi:10.1016/j.cirp.2017.05.011.
- [18] B. Zhang, Y. Li, Q. Bai, Defect Formation Mechanisms in Selective Laser Melting: A Review, *Chin. J. Mech. Eng.* 30 (2017) 515–527. doi:10.1007/s10033-017-0121-5.
- [19] Y.J. Liu, S.J. Li, H.L. Wang, W.T. Hou, Y.L. Hao, R. Yang, T.B. Sercombe, L.C. Zhang, Microstructure, defects and mechanical behavior of beta-type titanium porous structures manufactured by electron beam melting and selective laser melting, *Acta Mater.* 113 (2016) 56–67. doi:10.1016/j.actamat.2016.04.029.
- [20] C. Zhao, K. Fezzaa, R.W. Cunningham, H. Wen, F.D. Carlo, L. Chen, A.D. Rollett, T. Sun, Real-time monitoring of laser powder bed fusion process using high-speed X-ray imaging and diffraction, *Sci. Rep.* 7 (2017) 3602. doi:10.1038/s41598-017-03761-2.
- [21] S.K. Everton, M. Hirsch, P. Stravroulakis, R.K. Leach, A.T. Clare, Review of in-situ process monitoring and in-situ metrology for metal additive manufacturing, *Mater. Des.* 95 (2016) 431–445. doi:10.1016/j.matdes.2016.01.099.
- [22] M. Grasso, B.M. Colosimo, Process defects and in situ monitoring methods in metal powder bed fusion: a review, *Meas. Sci. Technol.* 28 (2017) 044005. doi:10.1088/1361-6501/aa5c4f.
- [23] J.A. Slotwinski, E.J. Garboczi, K.M. Hebenstreit, Porosity Measurements and Analysis for Metal Additive Manufacturing Process Control, *J. Res. NIST JRES - 119019.* (2014). <https://www.nist.gov/publications/porosity-measurements-and-analysis-metal-additive-manufacturing-process-control> (accessed June 26, 2018).
- [24] U. Hassler, D. Gruber, O. Hentschel, F. Sukowski, T. Grulich, L. Seifert, In-situ Monitoring and Defect Detection for Laser Metal Deposition by Using Infrared Thermography, *Phys. Procedia.* 83 (2016) 1244–1252. doi:10.1016/j.phpro.2016.08.131.
- [25] LaserForm Ti Gr23 (A), (2018). <https://www.3dsystems.com/sites/default/files/2018-03/3d-systems-laserform-ti-gr23%28a%29-datasheet-us-a4-2018.03.21-web.pdf>.
- [26] M. Bisht, N. Ray, F. Verbist, S. Coeck, Correlation of selective laser melting-melt pool events with the tensile properties of Ti-6Al-4V ELI processed by laser powder bed fusion, *Addit. Manuf.* 22 (2018) 302–306. doi:10.1016/j.addma.2018.05.004.
- [27] L. Thijs, F. Verhaeghe, T. Craeghs, J.V. Humbeeck, J.-P. Kruth, A study of the microstructural evolution during selective laser melting of Ti-6Al-4V, *Acta Mater.* 58 (2010) 3303–3312. doi:10.1016/j.actamat.2010.02.004.
- [28] H. Gu, H. Gong, D. Pal, K. Rafi, T. Starr, B. Stucker, Influences of Energy Density on Porosity and Microstructure of Selective Laser Melted 17-4PH Stainless Steel, 37 (2013) 474–489.
- [29] E. Liverani, S. Toschi, L. Ceschini, A. Fortunato, Effect of selective laser melting (SLM) process parameters on microstructure and mechanical properties of 316L austenitic stainless steel, *J. Mater. Process. Technol.* 249 (2017) 255–263. doi:10.1016/j.jmatprotec.2017.05.042.
- [30] ASTM E8 / E8M-16a, Standard Test Methods for Tension Testing of Metallic Materials, ASTM Int. West Conshohocken PA. (2016). doi:10.1520/E0008_E0008M-16A.
- [31] A.B. Spierings, M. Schneider, R. Eggenberger, Comparison of density measurement techniques for additive manufactured metallic parts, *Rapid Prototyp. J.* 17 (2011) 380–386. doi:10.1108/135525411111156504.
- [32] L.E. Murr, S.A. Quinones, S.M. Gaytan, M.I. Lopez, A. Rodela, E.Y. Martinez, D.H. Hernandez, E. Martinez, F. Medina, R.B. Wicker, Microstructure and mechanical behavior of Ti-6Al-4V produced by rapid-layer manufacturing, for biomedical applications, *J. Mech. Behav. Biomed. Mater.* 2 (2009) 20–32. doi:10.1016/j.jmbbm.2008.05.004.

- [33] B. Vrancken, L. Thijs, J.-P. Kruth, J. Van Humbeeck, Heat treatment of Ti6Al4V produced by Selective Laser Melting: Microstructure and mechanical properties, *J. Alloys Compd.* 541 (2012) 177–185. doi:10.1016/j.jallcom.2012.07.022.
- [34] L. Facchini, E. Magalini, P. Robotti, A. Molinari, S. Höges, K. Wissenbach, Ductility of a Ti-6Al-4V alloy produced by selective laser melting of prealloyed powders, *Rapid Prototyp. J.* 16 (2010) 450–459. doi:10.1108/13552541011083371.